weak forces. For example, van der Waals–Casimir forces might be measured by interferometrically observing changes in the tunneling characteristics as the microtraps are brought near a surface. However, possible systematic shifts arising from mean-field interactions would need to be characterized.

Study of transport in a regime with strong nonlinearities induced by the mean-field interactions is an interesting problem in its own right, with ties to the problem of phase-locking in Josephson arrays (*27*) and the Bose-Hubbard model (*28*). These nonlinearities might be exploited to generate and study squeezed states of the atom field. We expect that relatively straightforward modifications of our experimental parameters should enable quantitative studies in this regime.

The tunnel array output can also be viewed as an atom laser (*29*) whose coherence length (>500 μm) greatly exceeds the dimensions of the resonator. The time-domain pulses are directly analogous to the output of a mode-locked laser source (*30*), in which interference occurs between many properly phased continuous-wave output beams. The nearly constant time interval between successive pulses directly implies that the relative phase associated with each pulse envelope is well defined.

References and Notes

1. B. D. Josephson, *Phys. Lett.* **1**, 251 (1962); P. Anderson, *Basic Notions of Condensed Matter Physics* (Benjamin/Cummings, Menlo Park, CA, 1984), and references therein.
2. For recent interference experiments with coupled superfluid ^{3}He resevoirs, see S. Pereverzev, A. Loshak, S. Backhaus, J. Davis, R. Packard, *Nature* **388**, 449 (1997); S. Backhaus, S. V. Pereverzev, A. Loshak, J. C. Davis, R. E. Packard, *Science* **278**, 1435 (1997).
3. M. H. Anderson, J. R. Ensher, M. R. Matthews, C. E. Wieman, E. A. Cornell, *Science* **269**, 198 (1995); K. Davis *et al.*, *Phys. Rev. Lett.* **75**, 3969 (1995); C. Bradley, C. Sackett, J. Tollett, R. Hulet, *ibid.*, p. 1687.
4. D. S. Hall, M. R. Matthews, C. E. Wieman, E. A. Cornell, abstract available at http://xxx.lanl.gov/abs/cond-mat/9805327; M. R. Andrews *et al.*, *Science* **275**, 637 (1997).
5. A. Smerzi, S. Fantoni, S. Giovanazzi, S. Shenoy, *Phys. Rev. Lett.* **57**, 3164 (1997); I. Zapata, F. Sols, A. Leggett, *Phys. Rev. A* **57**, R28 (1998).
6. See, for example, A. Barone and G. Paternó, *Physics and Applications of the Josephson Effect* (Wiley, New York, 1982).
7. See, for example, J. Callaway, *Quantum Theory of the Solid State* (Academic Press, New York, ed. 2, 1991).
8. S. Wilkinson, C. Bharucha, K. Madison, Q. Niu, M. Raizen, *Phys. Rev. Lett.* **76**, 4512 (1996); Q. Niu, X. Zhao, G. A. Georgakis, M. Raizen, *ibid.*, p. 4504; M. Dahan, E. Peik, J. Reichel, Y. Castin, C. Salomon, *ibid.*, p. 4508.
9. C. Zener, *Proc. R. Soc. London Ser. A* **145**, 523 (1934).
10. Formally, the eigenstates are the Wannier-Stark states ψ_p, which are linear superpositions of the localized tight-binding (Wannier) states w_q: $\psi_p = \Sigma_q J_{q-p}(4T/mg\lambda)w_q$. Here J_n is the nth-order Bessel function, and T is the tunneling matrix element between lattice sites. See, G. Wannier, *Phys. Rev.* **117**, 432 (1961); H. Fukuyama, R. Bari, H. Fogedby, *Phys. Rev. B* **8**, 5579 (1973); D. Emin and C. Hart, *ibid.* **36**, 7353 (1987).
11. In this model, the position z_q^0 is offset by an arbitrary factor from the local lattice minimum. Because this offset is identical for each well, it amounts to a trivial spatial shift in the interference pattern.
12. Numerical solutions to the nonlinear Schrödinger equation indicate an oscillation amplitude of a few lattice sites for parameters used in our experiments.
13. B. Anderson and M. Kasevich, *Phys. Rev. A.*, in press.
14. E. Raab, M. Prentiss, A. Cable, S. Chu, D. Pritchard, *Phys. Rev. Lett.* **59**, 2631 (1987).
15. S. Chu, L. Hollberg, J. Bjorkholm, A. Cable, A. Ashkin, *ibid.* **58**, 48 (1985); P. Lett *et al.*, *ibid.* **61**, 169 (1988); J. Dalibard and C. Cohen-Tannoudji, *J. Opt. Soc. Am. B* **6**, 2023 (1989); P. Ungar, D. Weiss, E. Riis, S. Chu, *ibid.*, p. 2058.
16. W. Petrich, M. Anderson, J. Ensher, E. Cornell, *Phys. Rev. Lett.* **74**, 3352 (1995).
17. N. Masuhara *et al.*, *ibid.* **61**, 935 (1988).
18. B. Anderson, T. Gustavson, M. Kasevich, *Phys. Rev. A* **53**, R3727 (1996). See also, S. Friebel, C. D'Andrea, J. Walz, M. Weitz, T. Hänsch, *ibid.* **57**, R20 (1998); T. Müller-Seydlitz *et al.*, *Phys. Rev. Lett.* **78**, 1038 (1997).
19. See, for example, J. Gordon and A. Ashkin, *Phys. Rev. A* **21**, 1606 (1980). In the far-detuned limit, the potential is $\hbar\Omega_r^2/\Delta$, where Ω_r is the transition Rabi frequency and Δ is the detuning.
20. D. Stamper-Kurn *et al.*, *Phys. Rev. Lett.* **80**, 2027 (1998).
21. At our operating parameters, the photon scattering rate was <0.01 photon/s. From the probe absorption we infer a peak trap density of $\sim 10^{13}$ atoms/cm^3. Using the three-body loss coefficient from P. Fedichev, M. Reynolds, G. Shlyapnikov, *Phys. Rev. Lett.* **77**, 2921 (1996), we estimate a collision time of $\sim 4 \times 10^3$ s.
22. Phase space density is $n\lambda_{th}^3$, where $\lambda_{th} = \sqrt{2\pi\hbar^2/mk_BT}$ is the thermal de Broglie wavelength. Quantum degeneracy is realized for $n\lambda_{th}^3 > 1$. We inferred the temperature, T, from the spatial expansion of a pulse during the observation interval, and density, n, from the observed optical depth and spatial extent of the pulse (Fig. 4).
23. See, for example, G. Baym and C. Pethick, *Phys. Rev. Lett.* **76**, 6 (1996).
24. Note that turning on the optical potential adiabatically takes the condensate from the Thomas-Fermi regime (lattice potential off), where mean-field interaction energy dominates kinetic energy, to a regime where kinetic energy dominates the mean-field energy (lattice potential on).
25. See, for example, B. Taylor, W. Parker, D. Langenberg, *Rev. Mod. Phys.* **41**, 375 (1969).
26. For example, 10^7 atoms confined to a lattice with a 100-μm period would yield an acceleration sensitivity of $\sim 10^{-13}g$, assuming the atoms initially populate 10 wells and are observed to tunnel over a 100-s interval.
27. A. Jain, K. Likharev, J. Lukens, J. Sauvageau, *Phys. Rep.* **109**, 309 (1984).
28. D. Jaksh, C. Bruder, J. I. Cirac, C. W. Gardiner, P. Zoller, http://xxx.lanl.gov/abs/cond-mat/9805329.
29. M. Mewes *et al.*, *Phys. Rev. Lett.* **78**, 582 (1997).
30. A. Siegman, *Lasers* (University Science Books, Mill Valley, CA, 1986).

31. We thank M. Yasuda for technical assistance. Supported by the NSF and the Office of Naval Research.

13 August 1998; accepted 30 September 1998

Viscoelastic Flow in the Lower Crust after the 1992 Landers, California, Earthquake

Jishu Deng,* Michael Gurnis, Hiroo Kanamori, Egill Hauksson

Space geodesy showed that broad-scale postseismic deformation occurred after the 1992 Landers earthquake. Three-dimensional modeling shows that afterslip can only explain one horizontal component of the postseismic deformation, whereas viscoelastic flow can explain the horizontal and near-vertical displacements. The viscosity of a weak, about 10-km-thick layer, in the lower crust beneath the rupture zone that controls the rebound is about 10^{18} pascal seconds. The viscoelastic behavior of the lower crust may help to explain the extensional structures observed in the Basin and Range province and it may be used for the analysis of earthquake hazard.

The Landers M_w 7.3 earthquake is dominated by right-lateral strike-slip shear along four major multibranched fault segments (*1*) (Fig. 1A). Previous observations showed that postseismic deformation occurred in the local pull-apart basins or compressive jogs where two or more branches intersect on the surface (*2*). The local deformation within these fault structures can be explained by a time-dependent change in fluid pore pressure (*2*, *3*).

In addition to the fault-localized postseismic effects, broad-scale (for example about one to several fault lengths) postseismic deformation following the Landers earthquake has been observed by the global positioning system (GPS) and interferometric synthetic aperture radar (InSAR) measurements (*4*–*8*). The northern part of the earthquake rupture along the Emerson fault, moved in the horizontal direction perpendicular to the fault trace (fault-normal direction) for tens of millimeters (*4*) to the southwest. The GPS measurements (*4*) and InSAR images (*5*) also constrain postseismic rebound in the horizontal fault-parallel and near-vertical satellite line-of-sight (LOS) directions. Whether this broad-scale time-dependent rebound is driven by continuous afterslip below seismogenic depth on the fault plane (*4*, *8*, *9*) or by viscoelastic flow in the lower crust in response to the coseismic stress concentration (*10*–*13*) is not well understood. Savage (*14*) demonstrated the difficulty of distinguishing

Seismological Laboratory 252-21, California Institute of Technology, Pasadena, CA 91125, USA.

*To whom correspondence should be addressed. E-mail: jishu@gps.caltech.edu

between these two physical processes related to a long strike-slip fault from fault-parallel displacements taken at the surface. Compared to the viscoelastic relaxation model, the afterslip model is computationally easy to implement and is widely used to explain crustal deformation after major earthquakes (*4*, *8*, *9*, *15*). Because the coseismic rupture of the Landers earthquake involves three-dimensional effects such as fault curvature and nonuniform displacements, the postseismic patterns generated from the two models should be different and distinguishable. We developed three-dimensional viscoelastic models to explain the GPS observations (*4*) and InSAR measurements (*5*) after the 1992 Landers earthquake and to assess the postseismic processes and the physical properties of the crust.

About 2 weeks after the 28 June 1992 Landers earthquake, GPS receivers were deployed along a profile nearly perpendicular to the Emerson fault segment, where the largest coseismic rupture occurred (*4*) (Fig. 1A). Repeated observations in the following 3.4 years detected about 100 mm of right-lateral displacement and 50 mm of fault-normal motion across the 60-km-long profile. The GPS results also showed some systematic vertical movements with large uncertainties (*4*). The better constrained postseismic near-vertical displacements in the direction of LOS were observed by InSAR images obtained from the ERS-1 satellite (*5*). On the interferogram bracketing 2.75 years after the earthquake (Fig. 1A), a small area of 20 × 20 km to the west of the Emerson fault showed about 28 mm of subsidence, and a large area to the east of the whole rupture zone and to the west of the Johnson Valley fault showed 0 to 28 mm of uplift.

The Landers earthquake is generally believed to have ruptured mostly by strike-slip motion (for example, *16*, *17*). If the rupture was only accomplished by strike-slip motion, then although the afterslip and viscoelastic flow models can reproduce the horizontal fault-parallel component of the postseismic displacements (*14*), neither of the models can explain the observed horizontal fault-normal and near-vertical components. To model all components of the observations, some coseismic dip slip is necessary. There is evidence for a dip-slip component of motion on the Emerson fault segment (*18*).

Postseismic patterns related to a steep dip-slip fault or a strike-slip fault with a substantial dip-slip displacement can be used to distinguish between two rebound mechanisms, afterslip or viscoelastic flow (Fig. 2). The afterslip model, which assumes that the lower crustal part of the fault creeps aseismically with time at a decreasing rate of motion after a major earthquake (*15*), generates negligible fault-normal displacement proximal to the fault trace on the free surface. The viscoelastic relaxation model, which assumes that the postseismic deformation is driven by viscoelastic flow in a weak layer below the seismogenic zone in response to the coseismic stress concentration (*12*), produces a large horizontal fault-normal displacement

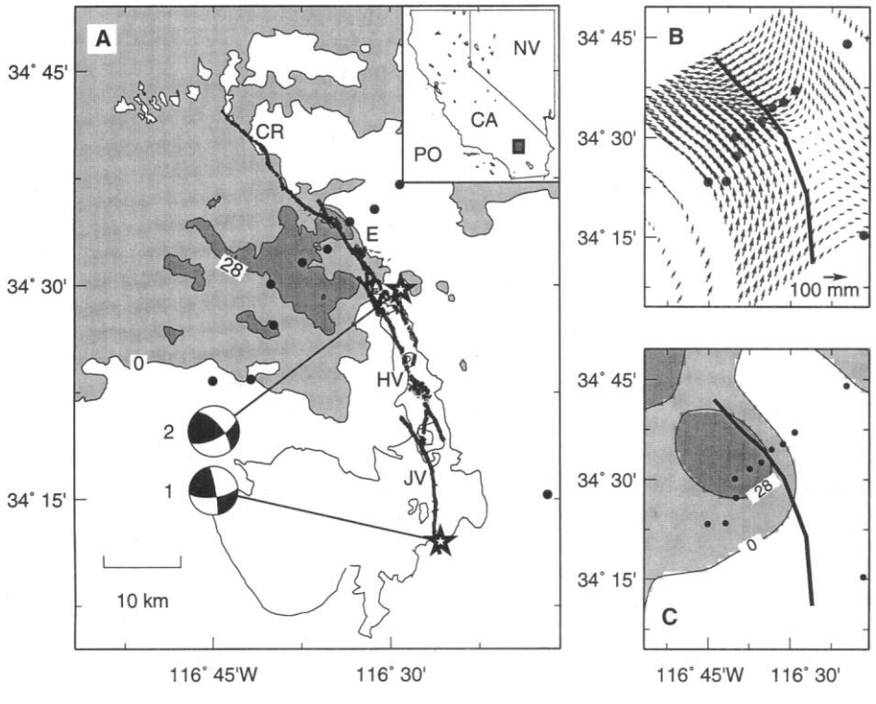

Fig. 1. (**A**) Rupture zone (*1*) and satellite-measured postseismic deformation (*5*) associated with the M_w 7.3 Landers earthquake of 1992. Focal mechanisms of the two subevents are from (*28*). Contour lines in millimeters represent distance changes of the ERS-1 satellite with respect to the ground surface, inferred from the combined InSAR interferogram bracketing a 2.75-year interval after the event. The radar antenna points to the Landers area at an azimuth of N77°W, with an average incidence angle of 23°. Areas that moved away from the satellite (subsidence) are shaded. Black dots indicate GPS stations (*4*). Fault segments: CR, Camp Rock fault; E, Emerson fault; HV, Homestead Valley fault; JV, Johnson Valley fault. (**B**) Postseismic displacement at part of the node points on the free surface computed using the viscoelastic model for the 3.4 years (the period bracketing the GPS measurements) after the Landers earthquake. (**C**) Range change away from the ERS-1 satellite for the 2.75 years after the earthquake predicted by the viscoelastic flow model.

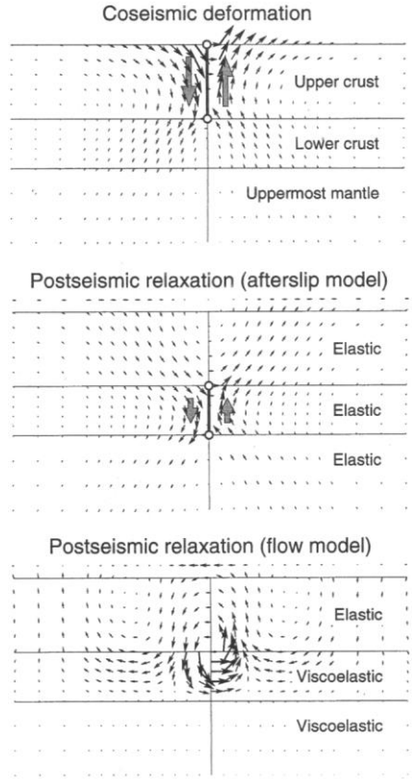

Fig. 2. Distribution of coseismic displacement related to a 2D vertical dip-slip dislocation and postseismic rebound predicted by afterslip and viscoelastic relaxation models. Heavy vertical lines and open circles indicate extents of edge dislocations. Large shaded arrows show dislocations across the fault planes. The horizontal component of the postseismic displacement on the surface is amplified by a factor of 1.5 and plotted on top of the cross sections. The deformation field of the afterslip model is generated by dislocation on the lower crust continuation of the fault. The viscoelastic rebound field is driven by viscoelastic flow in a weak lower crust for about two Maxwell times (the ratio between viscosity and shear modulus) since the earthquake, in response to the sudden coseismic stress concentration. The viscosity of the uppermost mantle is 100 times larger than that of the lower crust. The vertical offsets across the edge dislocation patches are not shown.

field on top of the fault trace, in the opposite direction of the coseismic displacement field. Both models produce some vertical displacements. Finite fault length and detailed slip distribution might make the postseismic signals more complicated than shown in Fig. 2.

We tried to match the GPS measurements of surface deformation along the profile in the 3.4 years following the earthquake with estimated deformation from three-dimensional (3D) afterslip and viscoelastic flow models. We applied two corrections to the horizontal components of the GPS measurements (*4*). First, we changed the reference point from Sandh (34.2550°N, 116.2789°W) to a remote station, Gold (35.4252°N, 116.8892°W), and removed the pre-Landers level of interseismic deformation associated with the San Andreas fault system, using the crustal velocity field released by the Southern California Earthquake Center (SCEC) (*19*). Second, we corrected the change in velocity at Gold before and after the earthquake using the continuous GPS measurements (*7*). The resulting horizontal displacements (Fig. 3) represent absolute postseismic deformation with respect to a fixed base line. The vertical component is calculated from the relative uplift rate (*4*). The GPS and InSAR measurements are combined to constrain the absolute vertical displacement of the third station from the northeast along the profile. All other stations are calibrated according to the constrained station so Fig. 3C shows absolute vertical displacements.

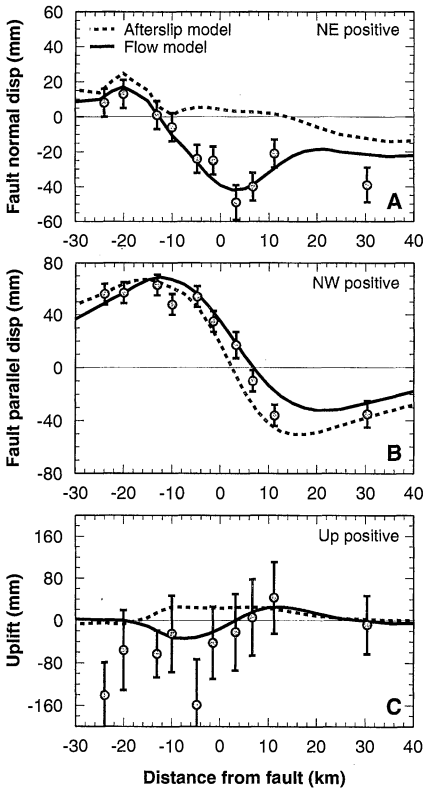

Fig. 3. Observed [shaded dots with 2-sigma error bars (*4*)] and calculated (dashed and solid lines) fault-normal (**A**), fault-parallel (**B**), and vertical (**C**) postseismic displacements along the GPS profile (distance to the northeast from fault is positive) in Fig. 1 for the 3.4 years after the Landers earthquake. Displacements are with respect to a fixed base line. The afterslip displacements were calculated for an elastic half space (*29*); the shear modulus and Poisson's ratio are 30 GPa and 0.25, respectively. Note that the afterslip and viscoelastic flow models can fit the fault-parallel component of the GPS measurements equally well, but only the viscoelastic flow model is consistent with the fault-normal component.

Viscoelastic flow calculations were performed using the finite element method. Our model consists of elastic and Maxwell viscoelastic materials, in which there can be vertical and lateral variations in material properties, with a free-surface on top and a heterogeneous fault surface embedded in a 3D cartesian space. An irregular 40 x 29 x 30 finite element grid covering 600, 600, and 300 km in northeast, northwest, and vertical directions was used to compute the time-dependent displacements (Figs. 1 and 3). The fault geometry was constrained by surface rupture measurements (*1*) and the distribution of aftershocks (*20*, *21*). The Emerson and Camp Rock segments of the fault dip 80° to the northeast. Strike-slip components of coseismic displacements are inferred from (*22*). Based on the evidence discussed earlier (*18*), we assumed 0.7 m of coseismic dip slip along the Emerson and Camp Rock segments, with an uncertainty range between 0.3 and 1.8 m. No dip-slip component is assumed for the Johnson Valley fault. The boundary between the upper and lower crust, which is at 15 km depth, is determined from the maximum depth of seismicity. The Moho depth is 28 km (*23*). All fault dislocations are confined to the upper crust. A 10-km weak layer of low viscosity in the middle of the lower crust is assumed to be responsible for the postseismic deformation. The rheology of the materials in the weak layer and below is assumed to be linear Maxwellian. The shear modulus is 30 GPa and Poisson's ratio is 0.25 for the crust and mantle. Viscosities of the weak layer and upper mantle are 10^{18} and 10^{20} Pa·s, respectively. The computer code FEVER (*24*) is used to calculate all viscoelastic relaxations in this study. The average amount of coseismic slip for each fault segment is assumed to take place in the lower crust in the afterslip model.

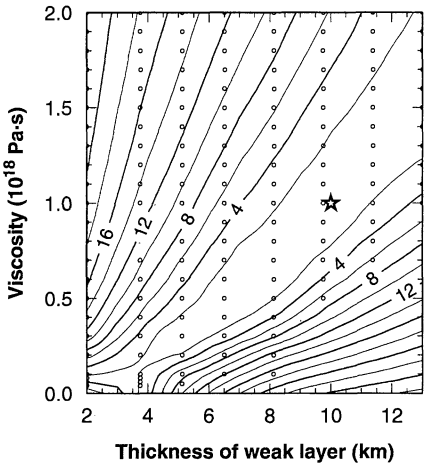

Fig. 4. Averaged absolute residuals of horizontal components of GPS measurements as a function of viscosity and thickness of the weak layer in the lower crust. Contour lines in millimeters are with respect to the minimum residual, 7 mm. Open circles indicate where actual calculations were performed. Star shows the set of parameters used to produce the flow results in Figs. 1 and 3.

The afterslip model and viscoelastic flow model can fit the fault-parallel component of the GPS measurements equally well (Fig. 3B). The afterslip model, however, cannot explain the fault-normal displacement (Fig. 3A). The averaged absolute residual of the afterslip model (24 mm) is 3 times larger than the estimated observational error (~8 mm). Other slip distributions might change the appearance of the curve slightly, but the fault-normal component on top of the fault trace cannot be modeled with any deep afterslip model, because the fault-normal displacement on top of the fault trace is not sensitive to displacement at depth in the lower crust. The viscoelastic relaxation model, on the other hand, explains the fault-parallel and fault-normal components, with an averaged absolute residual of 7 mm, which is consistent with the observed residual (Fig. 3A and B).

The vertical component of the GPS measurement is noisy (Fig. 3C) and cannot be used to distinguish between the two postseismic deformation models. Recent InSAR images, however, can test how these models work in the direction of the satellite, which is only 23° from vertical. From the work of Massonnet *et al.* (*5*), we show an interferogram bracketing 2.75 years after the earthquake (Fig. 1A). The general patterns of the subsidence to the west of the Emerson fault and uplift to the east of the whole fault trace detected by the inteferogram are consistent with the deformations derived from the viscoelastic model (Fig. 1C). The afterslip model predicts that both sides of the Emerson fault would be uplifted after the earthquake, which is inconsistent with the observed pattern.

Our calculations indicate that the viscoelastic flow model is consistent with the observed postseismic rebound following the Landers earthquake. The tradeoff between viscosity and the thickness of the weak layer constrained from the horizontal components of the GPS measurements is nearly linear (Fig. 4). The viscosity increases with the thickness of the weak layer in the lower crust. If the thickness is on the order of 10 km, the viscosity is around 10^{18} Pa·s. The InSAR

images, however, favor models with higher viscosities and thicker weak zones. The predicted deformation pattern (Fig. 1C) can match the observations (Fig. 1A) better if a weak zone of 13 km and a viscosity of 1.6 x 10^{18} Pa·s are used. Moreover, we find that the match between the InSAR images and model calculations can be improved if a nonuniform weak layer, (*24*), is used. The weak layer thickness at depth is determined from the geographical variations of the Moho depth (*23*). The calculated amplitude of uplift to the west of the Johnson Valley fault is closer to what is shown on the inteferogram (*25*).

A viscosity on the order of 10^{18} Pa·s in the lower crust is consistent with a maximum viscosity of the lower crust of 10^{19} Pa·s that is inferred from the uplift and tilting of Quaternary lake sediments on the Halloran Hills in the eastern Mojave desert (*26*). The weakness of the lower crust could be related to the thermal structure of the Basin and Range province, so it can help understand the physical mechanism responsible for the extension of the general area.

Our study on postseismic rebound does not resolve the mechanism responsible for interseismic deformation associated with major strike-slip faults (*27*). The postseismic deformation involves a sudden coseismic stress concentration close to the rupture zone, while the interseismic deformation only involves gradual strain concentration. So it is possible that a mechanism other than viscoelastic flow, such as stable sliding, is also related to the interseismic process (*27*).

Because viscosity governs the evolution of the stress field and thus the loading and unloading processes of major earthquake-generating faults, our estimate of the viscosity beneath the Landers earthquake region will help to assess earthquake hazards in southern California and further characterize the behavior of earhquake-related processes.

References and Notes

1. K. Sieh *et al.*, *Science* **260**, 171 (1993).
2. G. Peltzer *et al.*, *ibid.* **273**, 1202 (1996).
3. W. J. Bosl and A. Nur, *Eos* **78**, F491 (1997).
4. J. C. Savage and J. L. Svarc, *J. Geophys. Res.* **102**, 7565 (1997).
5. D. Massonnet, W. Thatcher, H. Vadon, *Nature* **382**, 612 (1996).
6. D. D. Jackson *et al.*, *Science* **277**, 1621 (1997).
7. Y. Bock *et al.*, *J. Geophys. Res.* **102**, 18013 (1997).
8. Z. K. Shen *et al.*, *Bull. Seismol. Soc. Am.* **84**, 780 (1994).
9. K. Heki, S. Miyazaki, H. Tsuji, *Nature* **386**, 595 (1997).
10. A. Nur and G. Mavko, *Science* **183**, 204 (1974).
11. J. B. Rundle, *J. Geophys. Res.* **83**, 5937 (1978); W. Thatcher and J. Rundle, *ibid.* **89**, 7631 (1984).
12. H. J. Melosh and A. Raefsky, *ibid.* **88**, 515 (1983); S. C. Cohen, *ibid.* **89**, 4538 (1984).
13. F. F. Pollitz, *ibid.* **102**, 17921 (1997).
14. J. C. Savage, *ibid.* **95**, 4873 (1990).
15. C. J. Marone, C. H. Scholtz, R. Bilham, *ibid.* **96**, 8441 (1991).
16. A. M. Dziewonski, G. Ekstrom, M. P. Salganik, *Phys. Earth Planet. Inter.* **77**, 151 (1993).
17. C. J. Ammon, A. A. Velasco, T. Lay, *Geophys. Res. Lett.* **20**, 97 (1993).
18. We note that the first-motion mechanism presented by Hauksson *et al.* (*20*) has a rake angle of 170° on a fault striking in N10°W. The mechanism solution of the second point source obtained by Qu *et al.* (*28*) (shown in Fig. 1), which is located near the southern end of the Emerson fault, has a rake angle of 153°, which involves even a larger dip-slip component than Hauksson *et al.*'s (*20*). Also several aftershocks near the Emerson fault show a significant thrust component (*20*). The aftershock distribution along the Emerson fault shown by figures 10a and 10b of (*20*) suggests a northeast dipping fault, which is qualitatively consistent with the solution of Qu *et al.* (*28*). F. Cotton and M. Campillo [*Geophys. Res. Lett.* **22**, 1921 (1995)] showed that the Landers earthquake is almost pure strike-slip, but the rake angle varies considerably around 180° on the Emerson and Camp Rock faults. Their average rake angle is about 176°. Surface rupture measurements [For example, J. R. Arrowsmith and D. D. Rhodes, *Bull. Seism. Soc. Am.* **84**, 511 (1994)] also showed some direct evidence of up to 2.5 m of vertical motion along a short segment of the Emerson fault. The various rake angles suggest that 7 to 45% of the seismic moment is released through dip-slip motion along the Emerson Fault segment, corresponding to 0.3 to 1.8 m of dip-slip displacement. In our calculations, we assume 0.7 m of dip-slip motion.
19. Z. K. Shen *et al.*, *Eos Trans. AGU* **78**, 477 (1997).
20. E. Hauksson, *et al.*, *J. Geophys. Res.* **98**, 19835 (1993).
21. E. Hauksson, *Bull. Seismol. Soc. Am.* **84**, 917 (1994).
22. D. J. Wald and T. H. Heaton, *ibid.*, p. 668.
23. K. B. Richards-Dinger and P. M. Shearer, *J. Geophys. Res.* **102**, 15211 (1997).
24. FEVER (Finite Element code for Visco-Elastic Rheology) is an object-oriented finite element software program developed by one of us (Deng). The code was implemented in C++ and systematically tested against many analytic solutions of linear and non-linear viscoelastic problems. The error of the numerical solution for almost all of the tested cases is within 1% of the corresponding analytic result.
25. We fixed the upper boundary of the weak zone to be 15 km deep, and assume that the lower boundary of the weak layer is the Moho surface, constrained from the Moho-reflected PmP arrivals (*23*). A thicker weak zone to the west of the Johnson Valley fault (Moho is about 32 km deep) (*23*) leads to a larger uplift rate in that region, compared to models with uniform Moho depth (28 km).
26. P. S. Kaufman and L. H. Royden, *J. Geophys. Res.* **99**, 15723 (1994).
27. L. E. Gilbert, C. H. Scholz, J. Beavan, *ibid.*, p. 23975.
28. J. Qu, T. L. Teng, J. Wang, *Bull. Seismol. Soc. Am.* **84**, 596 (1994).
29. Y. Okada, *ibid.* **82**, 1018 (1992); L. Erikson, User's manual for DIS3D: A three-dimensional dislocation program with applications to faulting in the earth, thesis, Stanford University (1986).

30. We thank M. Simons for a critical review of the manuscript and G. Peltzer, J. Savage, C. Scholz, K. Sieh, M. Spiegelman, L. Sykes, T. L. Teng, W. Thatcher, and many people in the seismo lab for discussion. This research was supported by SCEC. SCEC is funded by NSF Cooperative Agreement EAR-8920136 and USGS Cooperative Agreements 14-08-0001-A0899 and 1434-HQ-97AG01718. This is SCEC contribution 446 and contribution number 8574 of the Division of Geological and Planetary Sciences, California Institute of Technology.

17 August 1998; accepted 2 November 1998

In Search of the First Flower: A Jurassic Angiosperm, *Archaefructus*, from Northeast China

Ge Sun,* David L. Dilcher,* Shaoling Zheng, Zhekun Zhou

Angiosperm fruiting axes were discovered from the Upper Jurassic of China. Angiosperms are defined by carpels enclosing ovules, a character demonstrated in this fossil. This feature is lacking in other fossils reported to be earliest angiosperms. The fruits are small follicles formed from conduplicate carpels helically arranged. Adaxial elongate stigmatic crests are conspicuous on each carpel. The basal one-third of the axes bore deciduous organs of uncertain affinities. No scars of subtending floral organs are present to define the individual fertile parts as floral units, but the leaf-like structures subtending each axis define them as flowers. These fruiting axes have primitive characters and characters not considered primitive.

It has been thought that angiosperms first appeared about 130 million years ago in the Lower Cretaceous (*1, 2*). There are several recent reports of Triassic, Jurassic, and lowermost Cretaceous-aged fossils identified as angiosperms (*3–7*), but none of these reports can be accepted as conclusive evidence for the presence of angiosperms. Many reports of early angiosperms are based on pollen, leaves, and wood with vessels, none of which are definitive characters of angiosperms. Some are based on flowers and fruits that are too poorly preserved to demonstrate ovules or seeds enclosed in the carpels. The unique character of angiosperms is that the ovules

G. Sun, Nanjing Institute of Geology and Palaeontology, Academia Sinica, Nanjing 210008, China. D. L. Dilcher, Florida Museum of Natural History, University of Florida, Gainesville, FL 32611, USA. S. Zheng, Shenyang Institute of Geology and Mineral Resources, Shenyang 110032, China. Z. Zhou, Kunming Institute of Botany, Academia Sinica, Kunming 650204, China.

*To whom correspondence should be addressed. E-mail: gsun@jlonline.comi; dilcher@flmnh.ufl.edu